Evolution of ion beam induced patterns on Si(001)

Martin Engler,[1,*] Sven Macko,[1] Frank Frost,[2] and Thomas Michely[1]

[1] *II. Physikalisches Institut, Universität zu Köln, Cologne, Germany*

[2] *Leibniz-Institut für Oberflächenmodifizierung e. V., Leipzig, Germany*

(Received 7 March 2014; revised manuscript received 16 May 2014; published 9 June 2014)

In the range of incidence angles between 58° and 79°, Si develops erosion patterns through room-temperature exposure to 2 keV Kr^+, while for other incidence angles it remains flat. We investigate the formation of these patterns through all *in situ* sample preparation and investigation under ultrahigh vacuum conditions. The ion fluence is varied by a factor of 1000 for the incidence angles of 63° and 75°. The resulting morphologies are imaged by scanning tunneling microscopy and quantitatively analyzed in view of roughness, wavelength, disorder, and surface slopes. We find it necessary to distinguish between low-fluence and high-fluence regimes of pattern formation. While in both low-fluence regimes a similar parallel mode ripple pattern evolves, the high-fluence regimes are distinctly different and evidence either the evolution of disordered perpendicular ripples or a roof-tile structure for 63° or 75°, respectively. The data are compared to other experimental data for ion beam erosion of Si and Ge enabling us to assess the universality of our observations. Comparison to existing models for the surface evolution under ion exposure allows us to draw conclusions on the applicability of these models for pattern formation on Si(001).

DOI: 10.1103/PhysRevB.89.245412 PACS number(s): 68.37.Ef, 79.20.Rf, 81.16.Rf

I. INTRODUCTION

By now, pattern formation on surfaces through low-energy keV ions is known for more than 50 years [1]. The power of ion beams to create patterns rests on the ease by which large amounts of energy can be dissipated near the surface of materials, thereby, creating nonequilibrium, driven states of matter at the surface. They are determined by the interplay of energy dissipation and damage relaxation. Practically, patterning is simple and requires just to expose the sample to a plasma or an operating ion source such that energetic ions hit the sample. A rich variety of patterns has yet been observed [2–14], among them surprisingly regular ones [2,15]. The type of pattern that evolves does not only depend on the material exposed, but also on ion beam parameters (ion energy, ion species, angle of incidence) and temperature.

No single theory is able to capture the entire richness of patterns and their parameter space of formation. However, there are apparently simple, paradigmatic cases. First, at elevated temperatures, i.e., under conditions of rapid damage annealing, ion beam erosion of crystalline, elemental materials may be considered just as the inverse of homoepitaxial growth. As under these conditions a terrace step structure of the surface is maintained, pattern formation may be described by atomic scale processes invoking diffusion, nucleation, and kinetic effects hindering transport between different layers. This concept has been applied successfully in the past to explain pattern formation on low-index metal surfaces, e.g., on Pt(111) [3,16–22], but also semiconductors [9,23].

Second, ion beam erosion of amorphous materials, or materials that amorphize under the ion beam, must be considered to be well describable through continuum models neglecting the atomistic nature of matter. In this case, the power of partial differential equations may be exploited for the description of the height evolution. Bradley and Harper [24] introduced in 1988 a linear partial differential equation able to reproduce the observed ripple pattern rotation [1] from a ripple wave vector parallel to the wave vector perpendicular to the projection of the ion beam onto the surface with increasing ion incidence angle with respect to the surface normal.

Ion beam patterning of Si seemed to be an ideal test ground to develop the continuum approach of ion beam induced pattern formation: Si readily amorphizes during ion keV ion erosion, and it is a single-component material available in extreme purity and with a well defined flat starting surface. However, it was found that many early observations on pattern formation of Si were influenced by the presence of metallic impurities [4,25]. Once clean sputtering conditions were realized, an experimental consensus emerged that Si remains flat under ion beam exposure in a broad angular range [4,26,27]. Such a range of stability was inconsistent with the standard interpretation of the coefficients in the partial differential equations based on the Sigmund theory [28] of sputtering. It triggered substantial theoretical activity and resulted in a deeper understanding of the physical situation invoking now not only sputtering but also nonerosive material redistribution [29–33].

The last paragraph made it plain that in the past decade experimental ion beam erosion studies of Si surfaces played a central role in advancing our understanding of pattern formation. However, still, the experimental database of ion beam pattern formation on Si is incomplete. Specifically, there are only few fluence dependent studies, and these focus only on certain aspects of the morphological evolution. Madi *et al.* [34] and Castro *et al.* [31] investigate the onset of pattern formation, for low fluences or close to the critical angle for destabilization, Basu *et al.* [11] analyze a late stage of pattern formation for a specific angle of incidence while Keller *et al.* [35] and Zhang *et al.* [36] investigate the morphological evolution over an extended range of ion fluences, but only for a specific incidence angle.

Here we present a comprehensive study of low energy ion beam induced pattern formation on Si(001) identifying angular

*engler@ph2.uni-koeln.de

 ©2014 American Physical Society

ranges of incidence that differ markedly in morphological evolution and present for these ranges a qualitative and quantitative analysis spanning a factor of 1000 in ion fluence, starting from the initial stages of pattern formation. We exercise special care to obtain data characteristic for the single-component system, by starting ion exposure from a well defined initial state without the native oxide, by conducting ion exposure under ultrahigh vacuum conditions, and by using *in situ* analysis of the morphology through scanning tunneling microscopy. In our analysis, we link qualitative morphological evolution with quantitative analysis of roughness, characteristic wavelength, pattern order and slope distributions in the pattern. This methodology allows us to distinguish regimes of high- and low-fluence pattern evolution and to establish limits of applicability for the continuum description based on partial differential equations.

II. EXPERIMENTAL AND ANALYSIS

The ion erosion experiments were conducted in an ultrahigh vacuum (UHV) scanning tunneling microscopy (STM) system with a base pressure below 6×10^{-11} mbar. For the erosion experiments, the ion beam of a fine focus ion source was scanned over the sample with a time averaged ion flux of 4.2×10^{17} ions/(s m^2). During ion source operation, the pressure remained below 3×10^{-8} mbar and dropped below 1×10^{-10} mbar after the end of exposure. The ion flux was measured by a Faraday cup moved to the sample position. Ion fluences F are specified with respect to the sample plane, not to a plane perpendicular to the beam.

Si(001) pieces cut from a commercial n-doped wafer were transferred through a load lock into the UHV system. The samples were oriented such that the projection of the ion beam onto the sample coincided with the [110] direction in case of off-normal irradiation. In a first *in situ* preparation step, a fluence of 5×10^{20} ions/m^2 2 keV Kr^+ at normal incidence is used to completely remove the 1–3 nm thick oxide [37] and to amorphize the Si selvage. The resulting surface is smooth, with a roughness $\sigma \leqslant 0.3$ nm. In two sets of experiments, for angles of $\vartheta = 63^\circ$ and 75° with respect to the global surface normal, the sample was exposed to stepwise higher 2 keV Kr^+ fluences. After each exposure step, the sample was carefully characterized by *in situ* STM. After the terminal ion exposure at 75° resulting in a total fluence of 3×10^{22} ions/m^2, the sample was transferred out of vacuum and imaged by atomic force microscopy (AFM) as well as scanning electron microscopy (SEM).

The STM and AFM data were analyzed with the software WSXM [38], GWYDDION [39], and a custom programmed routine for the analysis of the slope angle distribution. First, a planar background was subtracted from each topograph. The distribution of the local slope angles of all surface area elements was then analyzed by calculating the polar angle α_{ij} of the local surface normal $\vec{n}_{ij}$, with respect to the global surface normal [compare Fig. 1(a)], and its azimuthal angle ϕ_{ij}. Using the angles α_{ij} and ϕ_{ij}, two-dimensional histograms for the slope angles were calculated. The size of the α intervals in the histograms were chosen such that the solid angle covered by each interval is constant. Figure 1(b) shows an example distribution. To determine the slope angles of the surface in ion beam direction, the slope angle distribution is cut along the ion beam direction as in Fig. 1(c). As *maximum* slope angle α_u (α_d) of the upwind (downwind) face such angles were chosen for which the intensity has dropped to half of its plateau value (or maximum value for the downwind face) as shown in Fig. 1(c). As the slope angle distribution is much broader for the upwind faces, we expect a considerably larger scatter for the values of α_u, as compared to the α_d, for which the downwind faces are distributed over a considerably narrower range of angles. Additionally, due to the steepness of the upwind faces for the 75°, the limited sharpness of the STM tip might also contribute to scatter.

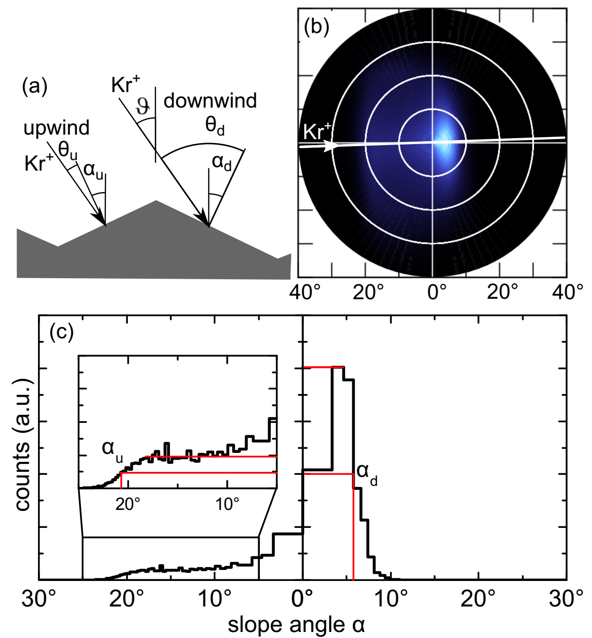

FIG. 1. (Color online) (a) Sketch of the sputtering geometry. The angles indicated are the ion incidence angle with respect to the normal of the global surface plane ϑ, the local slope angle α, and the local incidence angle θ. (b) Polar plot for the distribution of slope angles α. The direction of the ion beam is indicated by the white arrow. (c) Cut through the slope angle distribution of (b) along the ion beam direction with upwind (downwind) angles shown on the left (right). The maximum slope angle of the upwind (downwind) face is indicated by α_u (α_d). See text.

For the downwind face with the pronounced maximum in the slope angle distribution, alternatively, one might have picked the position of the maximum as a characteristic slope angle, resulting in values of α_d about 3° ($\vartheta = 75^\circ$) or 4° (for $\vartheta = 63^\circ$) smaller. However, there is no maximum in the slope angle distribution for the upwind face, implying an asymmetry in the evaluation of α_u and α_d with such a choice. The convention chosen here is unambiguous and emphasizes the maximal slopes present in the morphology.

By measuring for each experiment more than 100 distances λ_i between local maxima in profiles taken along the ion beam direction, the average wavelength $\lambda = \langle\lambda_i\rangle$ is calculated. For regular patterns, this procedure yields the same wavelength, as when calculated from the maximum of the Fourier transform of the image, but allows one to determine the mean lateral length of structures also in disordered patterns. The disorder

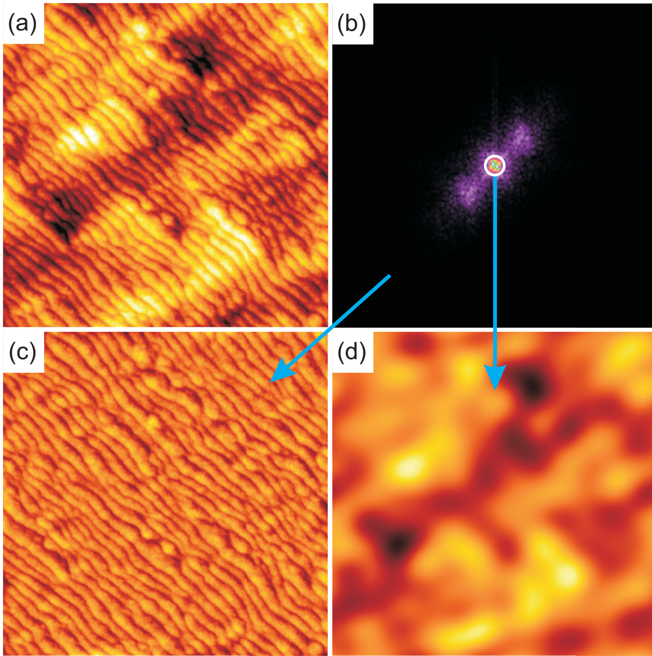

FIG. 2. (Color online) (a) STM topograph (image size 1.2 μm $\times$ 1.2 μm, z scale 9 nm) and (b) zoom into Fourier transform of (a) (limits $\pm 100\,\mu\text{m}^{-1}$). The blue circle with a radius $7\,\mu\text{m}^{-1}$ separates short-wavelength and long-wavelength components of the pattern. (c) Inverse Fourier transform of the short-wavelength component of (b) (z scale 6 nm). (d) Inverse Fourier transform of the long-wavelength component of (b) (z scale 9 nm).

of a pattern is quantified by the relative standard deviation of the wavelength $\delta\lambda/\lambda$, where $\delta\lambda$ is the standard deviation of the distances λ_i. The roughness of a surface is characterized by the root mean square (RMS) roughness σ.

To analyze the different ripple modes at $\vartheta = 63^\circ$, we separated the long-wavelength components with $1/\lambda < 7\,\mu\text{m}^{-1}$ from the short-wavelength components with $1/\lambda > 7\,\mu\text{m}^{-1}$ using a FFT filter as shown in Fig. 2. Starting from an STM topograph [Fig. 2(a)], its Fourier transform is calculated [Fig. 2(b)]. To separate short-wavelength and long-wavelength components of the pattern, within the Fourier transform, a circle around the origin is drawn. The low-frequency contribution inside of the circle and the high-frequency contribution outside of it are back transformed separately and represented in Figs. 2(c) and 2(d), respectively. As visible from Figs. 2(c) and 2(d), thereby a clear separation of the short-wavelength parallel ripple mode (wave vector of the ripple pattern parallel to the projection of the ion beam on the surface) and disordered, long-wavelength perpendicular ripples is achieved. The roughness obtained for Fig. 2(c) is defined as short-wavelength roughness σ_s, the one of Fig. 2(d) as long-wavelength roughness σ_l.

III. RESULTS

A. Angle dependence

To select proper ion incidence angles for our fluence dependent studies, for a fixed ion fluence $F = 1 \times 10^{22}$ ions/m^2 of 2 keV Kr$^+$ the sample morphology was analyzed (compare

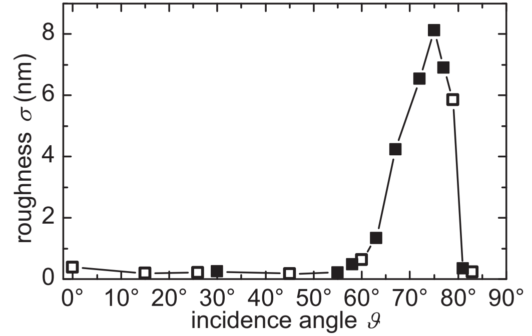

FIG. 3. Dependence of surface roughness σ on global ion incidence angle ϑ for fixed ion fluence $F = 1 \times 10^{22}$ ions/m^2 for 2 keV Kr$^+$. Data points represented as open squares (□) are taken from Ref. [4]. The typical error bar is smaller than the symbol size.

Fig. 3). We distinguish four morphological angular ranges: (i) the flat surface range for incidence angles $\vartheta \leqslant 55^\circ$. No pattern forms and the surface remains smooth with a surface roughness $\sigma < 0.4$ nm. (ii) The ripple pattern range for $58^\circ \leqslant \vartheta \leqslant 63^\circ$. The surface develops a parallel mode ripple pattern, of which the order increases with ϑ. Figure 4 shows the transition from the flat surface for $\vartheta \leqslant 55^\circ$ [Fig. 4(a)] to a rippled surface with $\vartheta \geqslant 58^\circ$ [compare Figs. 4(b)–4(d)]. The pattern quality improves with increasing incidence angle ϑ from 58° [Fig. 4(b)] via 60° [Fig. 4(c)] to 63° [Fig. 4(d)]. Additionally, with increasing ϑ disordered perpendicular ripples of large wavelength evolve that are well visible in Fig. 4(d) (see also Sec. II B). In this range, the roughness increases from $\sigma = 0.5$ nm at $\vartheta = 58^\circ$ to $\sigma = 1.3$ nm at $\vartheta = 63^\circ$. (iii) The roof-tile pattern range for $67^\circ \leqslant \vartheta \leqslant 79^\circ$. The surface morphology is dominated by an irregular parallel mode pattern that may be characterized as a roof tile structure (see also Sec. II C). The morphology is much rougher with $\sigma > 4$ nm and a maximum roughness of $\sigma \approx 8$ nm at $\vartheta = 75^\circ$. (iv) The grazing incidence range for $\vartheta \geqslant 81^\circ$. The surface is flat again with a roughness sigma below 0.4 nm and faint grooves in the direction of the ion beam. This morphology has been analyzed in more detail by Vivo *et al.* [40]. A detailed sequence of STM topographs visualizing the morphological evolution between $60^\circ \leqslant \vartheta \leqslant 81^\circ$ is provided as Fig. S1 in Ref. [41] (compare also Fig. 1 of Ref. [4]).

In conclusion, within an angular range of 26° four distinct morphologies are found, with clear fingerprints as specified above. The transition between two neighboring angular ranges is always sharp, in the sense that the transition range is defined by the angular steps in our angle dependent measurements. Thus, for the successive morphological angular ranges, we can specify angular intervals of transition that are less than 3° (flat surface to ripple pattern range), 4° (ripple pattern to roof-tile pattern range), and 2° (roof-tile pattern to grazing incidence range). There is no indication that the morphologies of the different angular ranges are transformable into each other by variations of ion fluence. This statement is obvious from the data shown, except for the transition from the ripple pattern to the roof-tile pattern, for which this issue is illuminated in more detail in the discussion below.

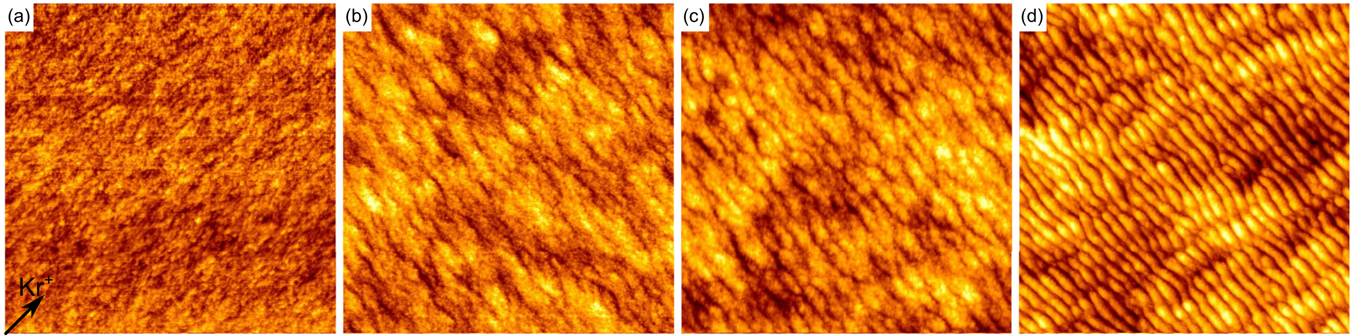

FIG. 4. (Color online) STM topographs ($1\,\mu$m $\times$ $1\,\mu$m) after a fluence of $F = 1 \times 10^{22}$ ions/m^2 2 keV Kr$^+$ with (a) $\vartheta = 55^\circ$, (b) 58°, (c) 60°, and (d) 63°. The wavelength decreases with increasing ϑ from $\lambda = (59 \pm 2)$ nm in (b) to $\lambda = (43 \pm 1)$ nm in (d). The z scales are (a) 2, (b) 3.4, (c) 4, and (d) 5 nm. The arrow in (a) indicates the direction of the ion beam.

For the flat surface range (i), no fluence dependence of the morphology down to the atomic scale could be detected. For the grazing incidence range (iv), only marginal variations of the morphology with ion fluence take place. Therefore we considered both ranges as unsuitable for a fluence dependent study. The morphological evolution in the ripple pattern (iii) and the roof-tile pattern (iv) ranges are the topic of the following sections.

B. Fluence dependence of morphology for 63° incidence angle

The STM topographs of Fig. 5 visualize the evolution of the surface topography with fluence during ion exposure with $\vartheta = 63^\circ$. The corresponding slope angle distributions are shown in Fig. 6. Figure 5(a) displays the initial state of the surface, after normal incidence ion beam amorphization of the surface near layer, prior to ion exposure at $\vartheta = 63^\circ$. The sample is smooth

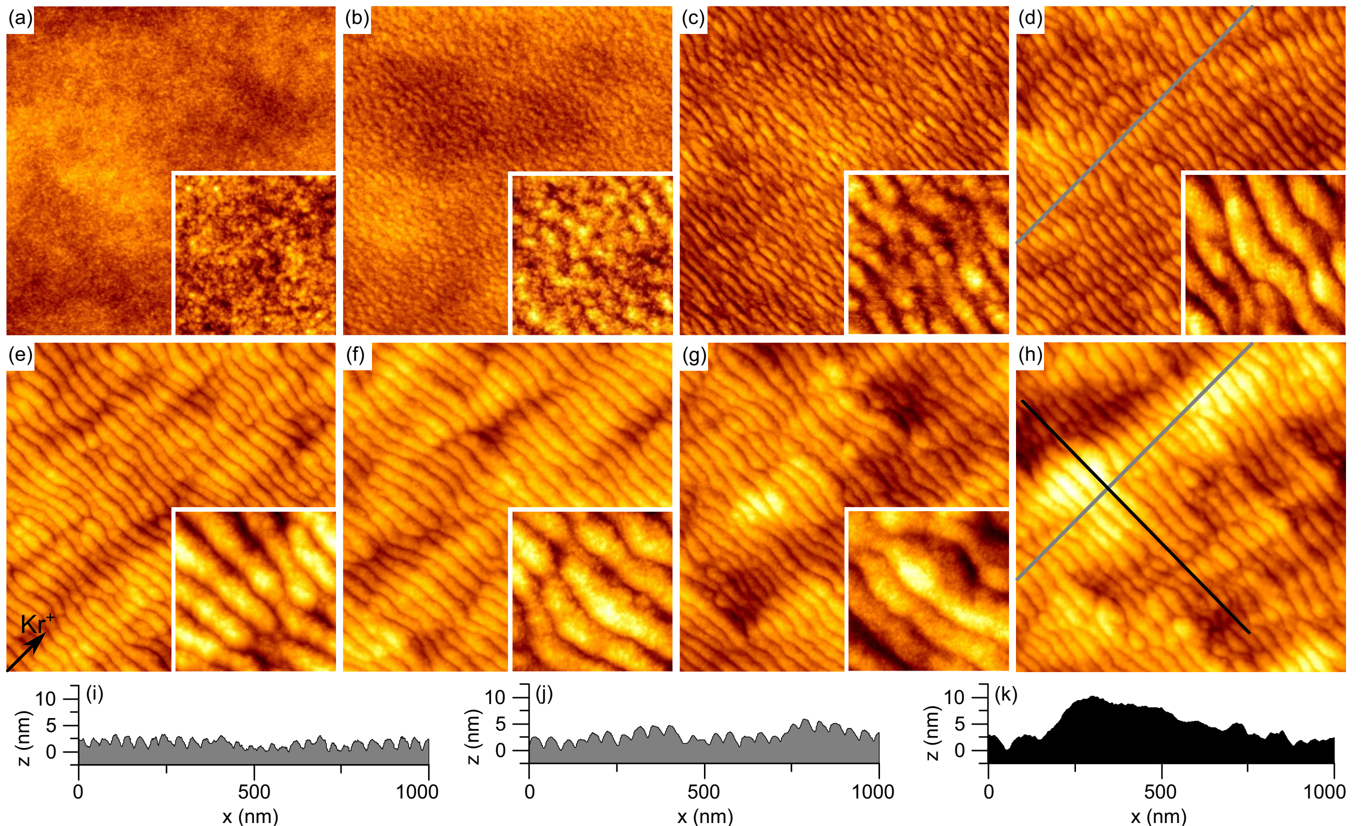

FIG. 5. (Color online) (a)–(h) STM topographs (image size $1\,\mu$m $\times$ $1\,\mu$m, inset size $0.2\,\mu$m $\times$ $0.2\,\mu$m) after 2 keV Kr$^+$ ion exposure with $\vartheta = 63^\circ$ and ion fluences increasing from (a) to (h): (a) initial state after removal of native oxide and normal incidence ion beam amorphization, no $\vartheta = 63^\circ$ ion exposure (z scale 4 nm), (b) $F = 1.0 \times 10^{20}$ (z scale 5 nm), (c) 3.0×10^{20} (z scale 5 nm), (d) 1.0×10^{21} (z scale 8 nm), (e) 3.0×10^{21} (z scale 10 nm), (f) 1.0×10^{22} (z scale 12 nm), (g) 3.0×10^{22} (z scale 12 nm), and (h) $F = 9.5 \times 10^{22}$ ions/m^2 (z scale 12 nm). The projected ion beam direction is indicated by the arrow in (e). (i) Height profile along a line parallel to ion beam direction as indicated in (d). (j) and (k) Height profiles along lines parallel and perpendicular to the ion beam direction, respectively, as indicated in (h). Note different scales for x and z that exaggerate the surface corrugation by a factor of more than 20.

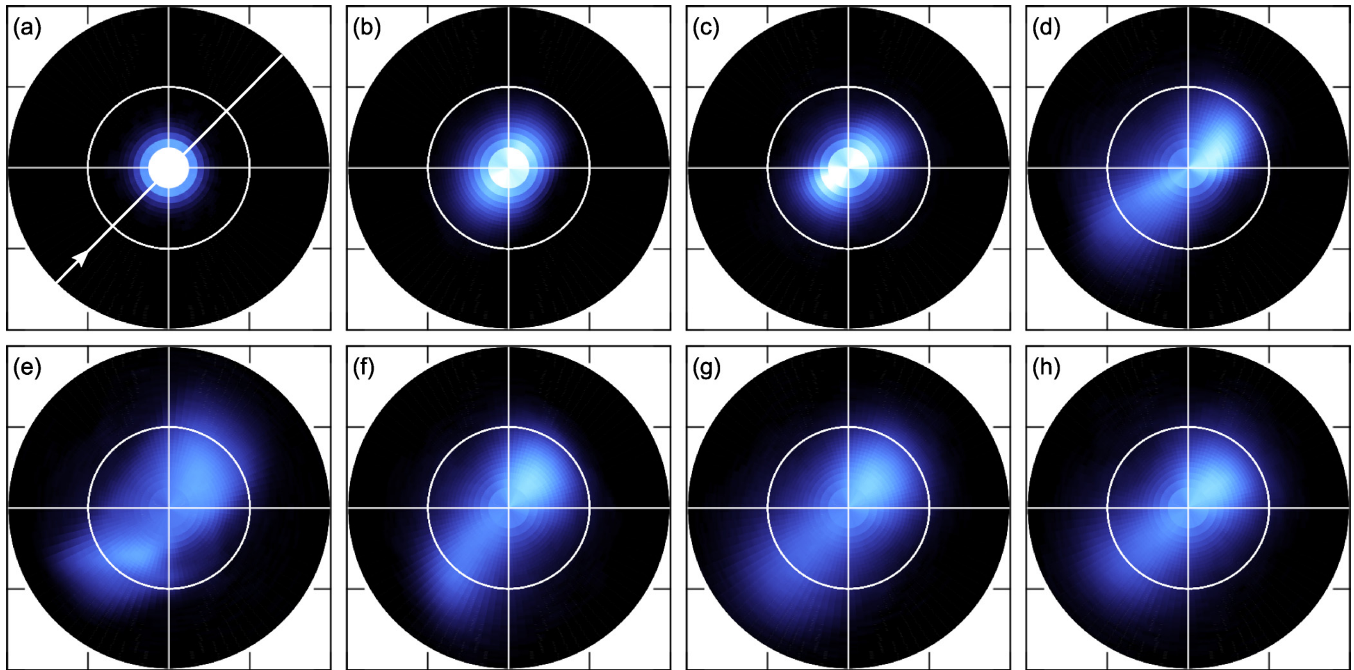

FIG. 6. (Color online) (a)–(h) Slope angle distributions of Figs. 5(a)–5(h). The slope angle varies from $\alpha = 0^\circ$ in the center to $\alpha = 20^\circ$ at the edge of the polar plot.

with weak height undulations on the micrometer range and atomic scale roughness related to the amorphization. The local slope angles are isotropically distributed in a narrow range around $\alpha = 0^\circ$ [compare Fig. 6(a)]. Upon ion exposure at $\vartheta = 63^\circ$ initially segmented, shallow ripples emerge [Fig. 5(b)] that merge to extended parallel mode ripples and increase in amplitude [Figs. 5(c)–5(d)]. The upwind and downwind ripple faces show equivalent local slope angles [Figs. 6(b)–6(c)] until the ripples become asymmetric for $F = 1.0 \times 10^{21}$ ions/m^2, as is obvious from Fig. 6(d) the pronounced downwind face has a smaller slope angle than the upwind face. At higher fluences, additional long-wavelength ripples with a wave vector perpendicular to the ion incidence direction emerge [Figs. 5(e)–5(h)], while the amplitude of the parallel ripple mode saturates.

The images acquired in the present study are too small in scale to identify, whether the long-wavelength ripples perpendicular to the ion beam direction acquire a characteristic wavelength, or whether they are just a broad range of undulations in that direction. The emergence of such perpendicular long-wavelength ripples at higher fluences has already been noted on Si(001) by Keller *et al.* [35] after 300 or 500 eV Ar$^+$ ion exposure at $\vartheta = 67^\circ$. By analysis of large AFM topographs Keller *et al.* [35] were able to attribute a characteristic wavelength to these ripples and classified them as a ripple mode. Based on this work, we will refer to these ripples in the following as a disordered perpendicular mode of ripples without being able to make an independent statement on whether a characteristic wavelength exists for these ripples. We note that such a perpendicular mode of disordered ripples has also been observed by Castro *et al.* [31] after 500 or 700 eV Ar$^+$ ion exposure at $\vartheta = 65^\circ$ or 70° as well as on Ge(001) by Teichmann *et al.* [42] after 600 eV Xe$^+$ ion exposure at $\vartheta = 65^\circ$.

The saturation of the parallel mode ripple pattern is rather obvious by comparison of the two height profiles along the ion beam direction [gray lines in Figs. 5(d) and 5(h)] shown in Figs. 5(i) and 5(j) for fluences of $F = 1.0 \times 10^{21}$ and 9.5×10^{22} ions/m^2, respectively. The profiles show a slight increase of the wavelength, but the shape and amplitude of the ripples change only marginally. The distribution of local slope angles parallel to the axis defined by the ion beam direction is similar at the fluences of $F = 1.0 \times 10^{21}$ ions/m^2 [Fig. 6(d)] and $F = 9.5 \times 10^{22}$ ions/m^2 [Fig. 6(h)]. However, perpendicular to this axis it becomes broader with increasing fluence, indicating the emergence of disordered perpendicular ripples modulating the height of the long-wavelength background of the ordered parallel ripples. Comparing the height profiles of Figs. 5(j) and 5(k) taken parallel and perpendicular to the ion beam direction [gray and black lines in Fig. 5(h)], after $F = 9.5 \times 10^{22}$ ions/m^2 shows that the amplitude of the disordered perpendicular mode is eventually larger than the one of the parallel mode. Figure 7 displays roughness σ, short-wavelength roughness σ_s, and long-wavelength roughness σ_l (see Sec. II for definitions of σ_s and σ_l). There is a characteristic change in the evolution of the roughness at $F = 3.0 \times 10^{21}$ ions/m^2: below this value, σ is dominated by σ_s resulting from the parallel mode ripples, while above it, is dominated by σ_l resulting from the disordered perpendicular mode. σ_s grows faster than σ_l until σ_s saturates at $F > 1.0 \times 10^{21}$ ions/m^2. σ_l continues to grow and crosses σ_s at $F = 3.0 \times 10^{21}$ ions/m^2. At this fluence, a disordered perpendicular mode with a length scale beyond 100 nm is clearly visible in the topography [Fig. 5(d)]. Above $F = 3.0 \times 10^{21}$ ions/m^2, the perpendicular modulations dominate σ. For comparison with the fluence dependent experiments for $\vartheta = 75^\circ$, σ is displayed as well in Fig. 8(a).

The evolution of the parallel mode ripple wavelength is shown in Fig. 8(b). The wavelength increases very slowly

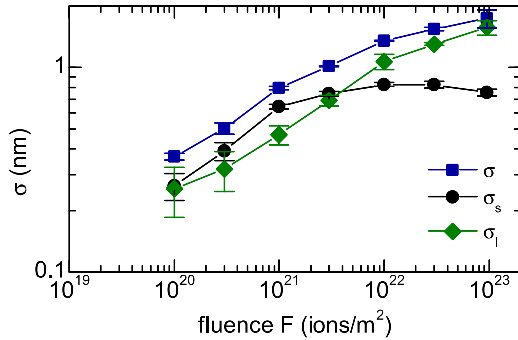

FIG. 7. (Color online) Evolution of the roughness σ, the short-wavelength roughness component σ_s, and the long-wavelength roughness component σ_l as a function of ion fluence F for $\vartheta = 63^\circ$.

with fluence from $\lambda = 31 \pm 1$ nm at $F = 3.0 \times 10^{20}$ ions/m^2 to $\lambda = 43 \pm 1$ nm at $F = 9.5 \times 10^{22}$ ions/m^2. The evolution of the ripple pattern disorder with fluence is plotted in Fig. 8(c). The pattern disorder $\delta\lambda/\lambda$ initially decreases, displays a minimum of $\delta\lambda/\lambda = 0.2$ for $F = 3.0 \times 10^{21}$ ions/m^2 and then increases again.

The fluence dependence of the local incidence angles θ_u and θ_d of the ion beam onto upwind and downwind faces, respectively, are shown in Fig. 8(d) by full blue symbols. θ_u and θ_d are calculated from the maximum slope angles of the upwind face α_u and the downwind face α_d via $\theta_u = \vartheta - \alpha_u$ and $\theta_d = \vartheta + \alpha_d$. For $F \leqslant 3.0 \times 10^{20}$ ions/m^2, the ripples are symmetric as is obvious from the equal separation of θ_u and θ_d from the blue line indicating the flat surface. Between $F = 3.0 \times 10^{20}$ and 1.0×10^{21} ions/m^2, the ripples become steeper and asymmetric: the upwind face tilts more towards the ion beam as the downwind face tilts away from it. The asymmetric ripple shape is stationary for $F \geqslant 1.0 \times 10^{21}$ ions/m^2 with $\theta_u \approx 52^\circ$ corresponding to a maximum slope angle $\alpha_u \approx 11^\circ$ and $\theta_d \approx 71^\circ$ corresponding to a maximum slope angle $\alpha_d \approx 8^\circ$.

It is tempting to summarize the results of our qualitative and quantitative analysis by distinguishing two regimes in the evolution of the morphology at ion irradiation with $\vartheta = 63^\circ$: a low-fluence regime with $F \leqslant 1 \times 10^{21}$ ions/m^2 and a high-fluence regime $F \geqslant 3 \times 10^{21}$ ions/m^2. The transition between the two regimes is gradual and therefore it is highlighted in Fig. 8 through the light blue shaded vertical bar in the fluence range 1×10^{21} ions/m$^2 \leqslant F \leqslant 3 \times 10^{21}$ ions/m^2. In the low-fluence regime, only a parallel ripple mode is present. The corresponding ripple amplitude grows, the pattern wavelength is almost constant, the pattern disorder decreases and the ripple profile steepens while changing from a symmetric to an asymmetric one with increasing fluence. In the high-fluence regime, a disordered perpendicular mode evolves that eventually dominates the roughness. At the same time, the wavelength and profile of the parallel ripple mode become stationary. In consequence of the growth of the disordered perpendicular mode, also the disorder in the parallel mode ripples increases.

C. Fluence dependence of morphology for 75° incidence angle

The STM and AFM topographs of Fig. 9 visualize the evolution of the surface topography with fluence during ion exposure with $\vartheta = 75^\circ$. The corresponding slope angle distributions are

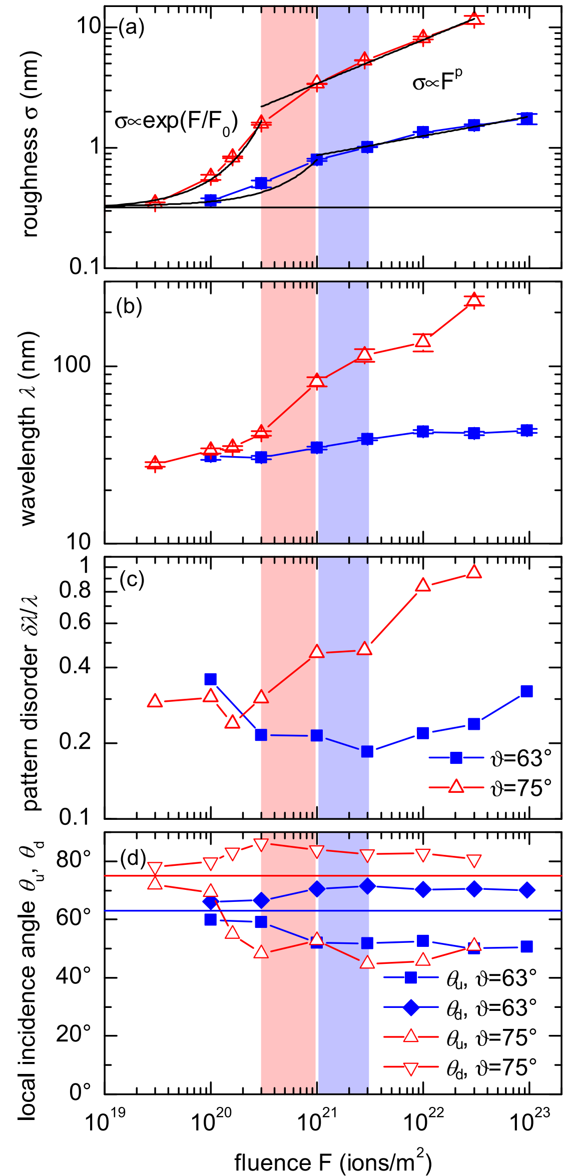

FIG. 8. (Color online) Evolution of (a) roughness σ, (b) wavelength λ, (c) pattern order $\delta\lambda/\lambda$, and (d) local ion incidence angle θ_u on upwind and θ_d on downwind ripple faces. In (a), the horizontal line indicates the sample roughness prior to off-normal ion exposure. In (d), the horizontal lines indicate the global incidence angles. The transition range between the low-fluence and high-fluence regimes is highlighted by the light blue shaded area for the $\vartheta = 63^\circ$ experiments and by the light red shaded area for the $\vartheta = 75^\circ$ case.

shown in Fig. 10. Already, for $F = 3.0 \times 10^{19}$ ions/m^2, the grainy surface displays a characteristic separation [Fig. 9(a)]. The corresponding slope angles are still isotropically distributed as apparent in Fig. 10(a). This structure transforms into a ripple pattern [compare Fig. 9(b)], still symmetric in slope angle distribution [compare Fig. 10(b)]. Compared to the 63° case, for the same fluence of $F = 1.0 \times 10^{20}$ ions/m^2 at 75° the pattern is better developed. By increasing the ion fluence, this initial pattern dramatically grows in amplitude and strongly coarsens [compare Figs. 9(c)–9(f) and height profiles Figs. 9(i)–9(k)]. Well defined downwind faces develop

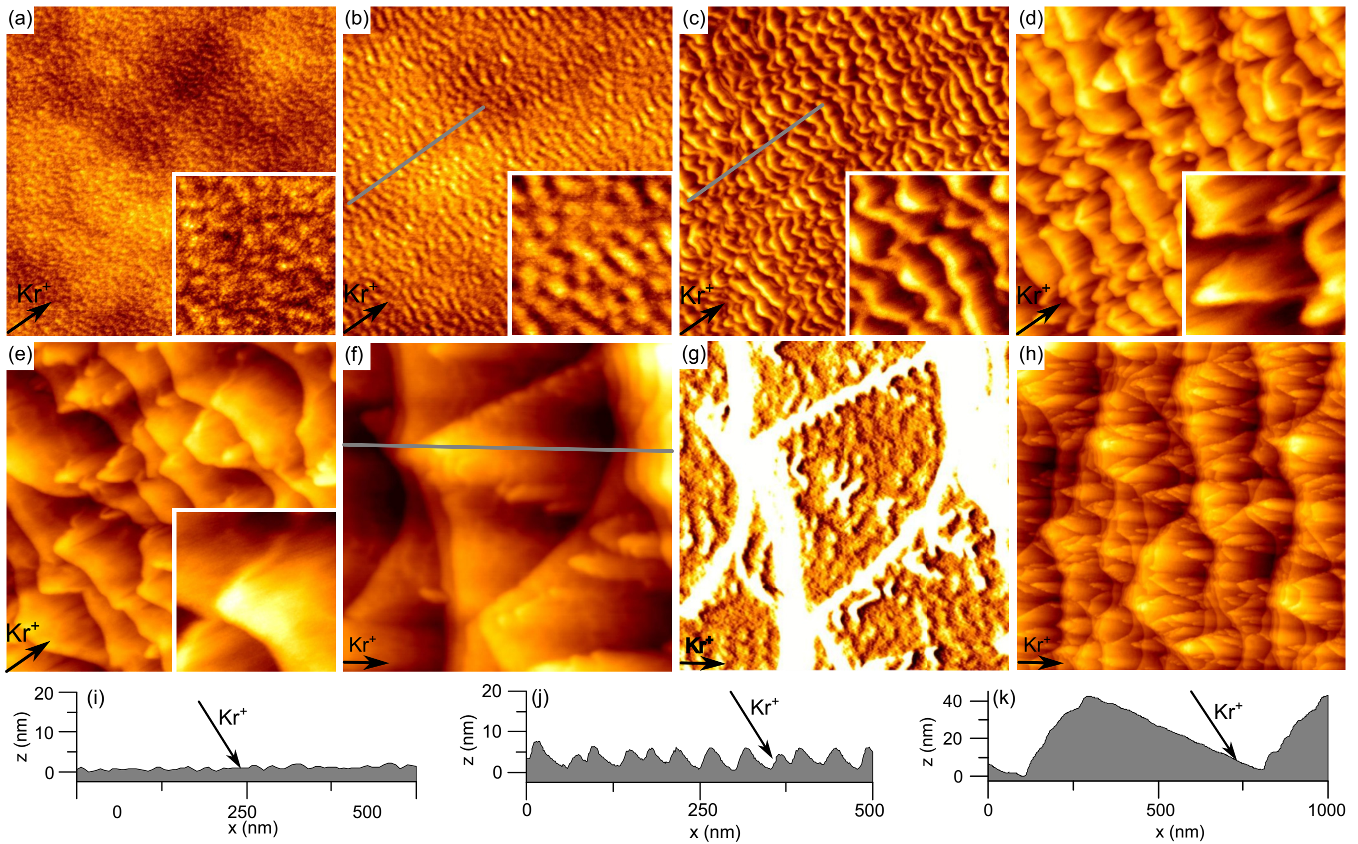

FIG. 9. (Color online) (a)–(e) *In situ* STM topographs and (f) *ex situ* AFM image (image size 1 μm × 1 μm, inset size 0.3 μm × 0.3 μm) after 2 keV Kr^+ ion exposure with $\vartheta = 75^\circ$ after ion fluences of (a) $F = 3.0 \times 10^{19}$ (z scale 10 nm), (b) 1.0×10^{20} (z scale 20 nm), (c) 3.0×10^{20} (z scale 20 nm), (d) 1.0×10^{21} (z scale 30 nm), (e) 3.0×10^{21} (z scale 35 nm), and (f) 3.0×10^{22} ions/m^2 (z scale 70 nm). (g) Derivative of (f) in horizontal direction that highlights the corrugation on downwind faces. (h) Large scale *ex situ* AFM 5 μm × 5 μm image after $F = 3.0 \times 10^{22}$ ions/m^2 (z scale 100 nm). The projected ion beam direction is indicated by an arrow in each case. (i)–(k) Height profiles along lines parallel to ion beam direction as indicated in (b), (c), and (f), respectively. Note different scales for x and z that exaggerate the surface roughness by a factor of 5.5. Arrows indicate the direction of ion beam incidence properly scaled.

[Figs. 10(c)–10(f)] that appear in the topographs as large, terracelike areas separated by the steep, steplike upwind faces. Initially, the ridge line of the ripples is wavy with some v-shaped tips [Fig. 10(c)]. With increasing fluence [Figs. 10(d)–10(f)] v-shaped tips pointing in the direction of the ion beam become more prominent. The downwind faces develop grooves in the ion beam direction leading to a broadening of the slope angle distribution perpendicular to the ion beam direction [most pronounced in Fig. 10(d)]. The pattern becomes less regular as short and long downwind faces are formed. At the fluence of $F = 3.0 \times 10^{22}$ ions/m^2 [Figs. 9(f) and 9(h)], the downwind faces—the extension of the tiles in the roof-tile structure—amount up to 1 μm length. They display a local incidence angle of $\theta_d = 82^\circ$ and are often separated by stairlike bunches of alternating upwind and downwind faces. An additional ripple pattern with a periodicity of ≈50 nm on the extended downwind faces is highlighted by the derivative Fig. 9(g). We note that strong coarsening and the formation of a roof-tile structure has already been observed by Zhang *et al.* [36] after 5 keV Xe^+ exposure at $\vartheta = 80^\circ$ on Si(001), by Basu *et al.* [11] after 500 eV Ar^+ exposure at $\vartheta = 72.5^\circ$ on Si(001), and by Teichmann *et al.* [42] after 1.2 keV Kr^+ and Xe^+ exposure at $\vartheta = 75^\circ$ on Ge(001).

The evolution of the surface roughness is plotted in Fig. 8(a). Compared to the 63° case, σ increases much faster with F for the 75° case. Initially, for $F < 1.0 \times 10^{21}$ ions/m^2, the roughness displays exponential growth and can be fitted by $\sigma \propto \exp(F/F_0)$ with $F_0 = (1.8 \pm 0.1) \times 10^{20}$ ions/m^2. For higher fluences, σ displays a power-law behavior $\sigma \propto F^p$ with $p = 0.36 \pm 0.03$. Also for the 63° case, a power-law behavior may be fitted to the high-fluence regime, while an exponential fit to the low-fluence data yields only a moderate match [compare Fig. 8(a)].

Initially, up to a fluence of $F = 3.0 \times 10^{20}$ ions/m^2, the characteristic feature separation along the ion beam direction (wavelength) increases only moderately with F [compare Fig. 8(b)] and the pattern disorder $\delta\lambda/\lambda$ remains below 0.3 [Fig. 8(c)]. Beyond this critical fluence, a rapid coarsening up to the highest analyzed fluences is observed, in striking contrast to the 63° case. This coarsening coincides with a dramatic increase in pattern disorder, apparently beyond any bound.

The fluence dependence of the local incidence angles θ_u and θ_d of the ion beam onto upwind and downwind faces, respectively, are shown Fig. 8(d) as red triangles. Up to the critical fluence of $F = 3.0 \times 10^{20}$ ions/m^2, the faces of the pattern disperse away from the red line in Fig. 8(d) that

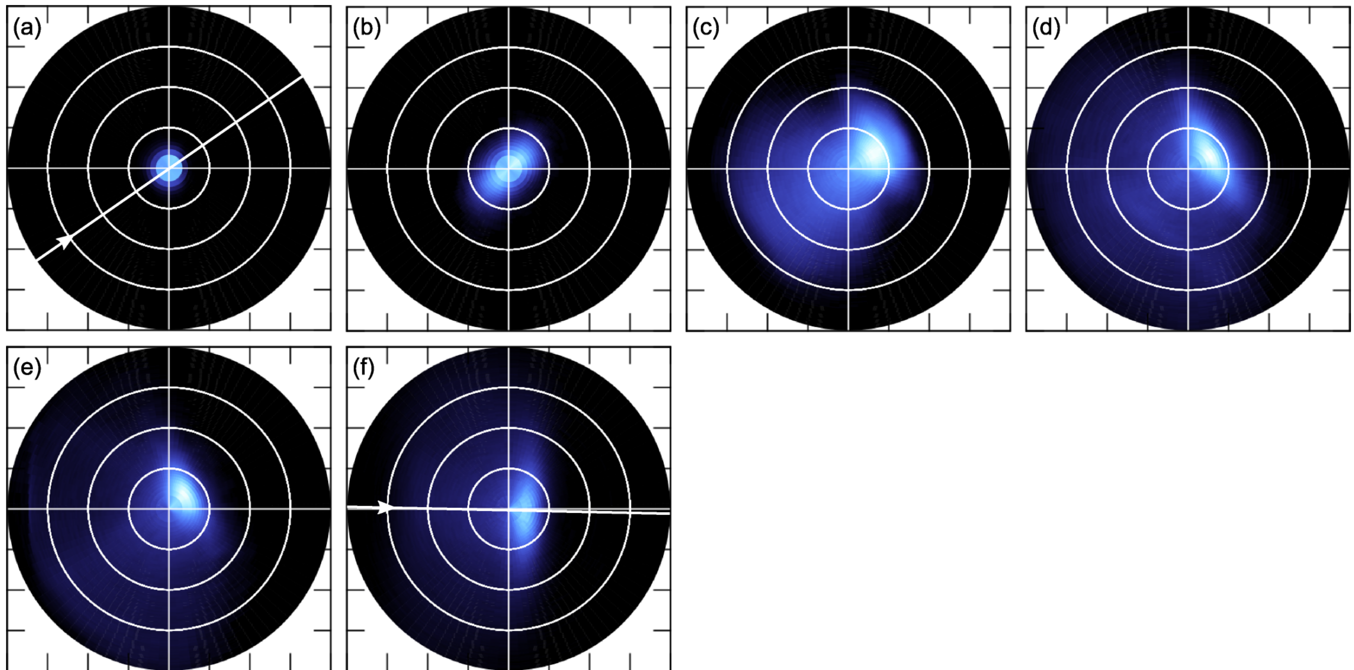

FIG. 10. (Color online) (a)–(h) Slope angle distributions of Figs. 9(a)–9(f). The slope angle varies from $\alpha = 0^\circ$ in the center to $\alpha = 40^\circ$ at the edge of the polar plot.

indicates the flat surface. Only up to $F = 1.0 \times 10^{20}$ ions/m^2 this dispersal is symmetric. During subsequent ion exposure, the upwind face moves much farther away from the flat surface than the downwind face. Therefore the pattern is asymmetric, as is also obvious from the topographs Figs. 9(c)–9(f). Beyond the critical fluence of $F = 3.0 \times 10^{20}$ ions/m^2 the incidence angles are $\theta_u \approx 50^\circ$ corresponding to a slope angle $\alpha_u \approx 25^\circ$ and $\theta_d \approx 82^\circ$ corresponding to $\alpha_d \approx 8^\circ$, consistent with the absence of a significant variation in the slope angle distributions [Figs. 10(d)–10(f)].

To summarize, also for the $\vartheta = 75^\circ$ case, we may distinguish two regimes of morphological evolution: a low-fluence regime with $F \leqslant 3 \times 10^{20}$ ions/m^2 and a high-fluence regime $F \geqslant 1 \times 10^{21}$ ions/m^2. The transition between the two regimes is gradual and highlighted in Fig. 8 through the light red shaded vertical bar in the fluence range 3×10^{20} ions/m^2 $\leqslant F \leqslant 1 \times 10^{21}$ ions/m^2. Compared to the 63° case, the transition is shifted to lower F. In the low-fluence regime, a parallel ripple mode quickly emerges. The corresponding ripple amplitude grows exponentially, the pattern coarsens slightly, the pattern disorder is essentially constant around 0.3 and the ripple profile steepens and develops well oriented faces while changing from a symmetric to an asymmetric one with increasing fluence. In the high-fluence regime, the resemblance to a parallel mode ripple pattern is lost and a roof-tile pattern emerges. Strong coarsening and pattern disordering is found, while the local incidence angles develop stationary values characterizing a surface topography of well defined faces.

IV. DISCUSSION

For both incidence angles, $\vartheta = 63^\circ$ and 75°, two distinct regimes of surface morphological evolution are identified in our experiments. The gradual transition between the two regimes shifts with increasing ϑ to lower ion fluence by about a factor of 3. The key features of the two different fluence regimes are summarized in Table I for $\vartheta = 63^\circ$ and in Table II for $\vartheta = 75^\circ$. The low-fluence regimes display similar properties for both incidence angles, while the high-fluence regimes are qualitatively different for them.

We consider the low-fluence regimes to reasonable approximation as realizations of a linear instability, as it is usually described by a linear partial differential equation of the form first given by Bradley and Harper [24]:

$$\partial_t h = -v_0(\vartheta) + B\partial_x h + v_x \partial_x^2 h + v_y \partial_y^2 h - K\nabla^4 h. \quad (1)$$

Here, v_0 is the erosion speed of a flat surface, $B = \partial_\theta v_0$ is the dependence of the erosion speed on the local incidence angle θ, v_x, and v_y are the curvature depending terms, and K is the surface relaxation due to the minimization of the surface tension. Two effects may contribute to v_x and v_y—the curvature dependence of the erosion speed as shown in the work of Bradley and Harper [24] and mass redistribution as it results from the Carter-Vishnyakov effect [29], ion induced solid flow [30,31], or the crater function approach [32,33]. All linear theories [24,30,32,33,43–45] based on Eq. (1) predict for sufficiently low ϑ and for the case of an instability, i.e., $v_x < 0$, that $v_x < v_y$, i.e., a parallel mode ripple pattern with an exponential increase of roughness and a well defined wavelength to evolve. One expects the disorder of the pattern to decrease with ion fluence, as the fastest growing wavelength will eventually dominate the morphology. In fact, experimentally, we observe in the low-fluence regimes, parallel mode ripple patterns. Their roughness increase can be fitted moderately ($\vartheta = 63^\circ$) or quite well ($\vartheta = 75^\circ$) as exponential growth of the pattern amplitude [compare Fig. 8(a)]. The ripple patterns display a well defined wavelength with hardly

TABLE I. Regimes of morphological evolution at $\vartheta = 63^\circ$.

	Low-fluence regime	High-fluence regime
fluence F	$\leqslant 1.0 \times 10^{21}$ ions/m^2	$\geqslant 3.0 \times 10^{21}$ ions/m^2
morphology	parallel mode ripples	disordered perpendicular mode + parallel mode ripples
roughness σ_s, σ_l	σ_s increases σ_l increases slowly	σ_s constant σ_l increases
slope angles α_d, α_u	increase	constant
wavelength λ	slight coarsening	slight coarsening
$\frac{\delta\lambda}{\lambda}$	decreases	increases

any ($\vartheta = 63^\circ$) or only slow coarsening ($\vartheta = 75^\circ$) [compare Fig. 8(b)]. The observed pattern disorder decreases with ion fluence as expected ($\vartheta = 63^\circ$) or, at least, it does not increase ($\vartheta = 75^\circ$) [compare Fig. 8(c)]. We note that the low-fluence regimes should only be considered as *approximate* realizations of a linear instability, as indicated by the slight deviations from the expected behavior, e.g., the slow coarsening for $\vartheta = 75^\circ$.

Our observations are at variance in two aspects with models based on the Sigmund theory of sputtering [28], like the Bradley-Harper model [24] and extensions of it [43,44]. First, we observe no ripple rotation from parallel mode ripples to perpendicular mode ripples with increasing ϑ. The ripple rotation with increasing ϑ has been observed experimentally for other systems [13] and the ability of the Bradley-Harper-type models to reproduce this ripple rotation was key to their acceptance as a valid description of ion beam induced pattern formation.

Second, ripples emerge only for angles larger than a critical angle, in the present case for $\vartheta > 55^\circ$. The emergence of ripples only for incidence angles greater than the critical angle can be explained by models taking mass redistribution into account, either by ballistic mass drift [29], by solid flow [30,31], or by the average crater functions of single impacts [32,33]. In the hydrodynamic model of Castro and Cuerno [30], the assumption of an ion-induced "effective body force" $b \propto \cos\theta$ leads to the prediction of a transition from a flat surface near normal incidence to a rippled surface at $\vartheta = 45^\circ$, independent of ion energy and species, like in the ballistic mass drift model of Carter and Vishnyakov [29]. Apparently, modifications in the description of the body force would be necessary to explain the transition from a flat to a rippled surface between $\vartheta = 55^\circ$ and 58°. Mass redistribution is also inherently incorporated in the crater function approach by Norris *et al.* [32,33] that is based on obtaining the moments of a crater function as deduced by averaging over many impacts simulated by molecular dynamics (MD). For 250 eV Ar^+ exposure, the transition from a flat to a rippled surface is predicted to take place at $\vartheta = 40^\circ$. The match of this approach to the present situation can only be judged if the MD simulations are extended to higher energies and to heavier projectiles.

TABLE II. Regimes of morphological evolution at $\vartheta = 75^\circ$.

	Low-fluence regime	High-fluence regime
fluence F	$\leqslant 3.0 \times 10^{20}$ ions/m^2	$\geqslant 1.0 \times 10^{21}$ ions/m^2
morphology	parallel mode ripples	roof-tile structure
roughness σ	exponential growth	power-law growth
slope angles α_d, α_u	increase	constant
wavelength λ	slow coarsening	fast coarsening
$\frac{\delta\lambda}{\lambda}$	constant	increases

Based on the ion induced solid flow model, Castro *et al.* [31] predict an intrinsic time scale τ that limits the description of the morphological evolution through a linear partial differential equation. It scales with ϑ as $\tau(\vartheta) \propto 1/\cos^2(2\vartheta)$, i.e., with increasing ϑ shifts to smaller F. The predicted ratio of the time scales for our experiments is $\tau(63^\circ)/\tau(75^\circ) = 2.2$, which corresponds to a ratio of fluences $F(63^\circ)/F(75^\circ) = 3.8$. In fact, experimentally, we find $F(63^\circ)/F(75^\circ) \approx 3$ in reasonable agreement with the prediction of the solid flow model (compare Fig. 8).

Next, we discuss the high-fluence regime for $\vartheta = 63^\circ$. The saturation of the short-wavelength mode observed at $F = 1.0 \times 10^{21}$ ions/m^2 (compare Fig. 7) is clearly a nonlinear effect. A simple nonlinear partial equation able to describe the saturation of one mode is the anisotropic Kuramoto-Sivashinsky equation (aKS equation) [46]

$$\partial_t h = \nu_x \partial_x^2 h + \nu_y \partial_y^2 h - K\nabla^4 h + \frac{\lambda_x}{2}(\partial_x h)^2 + \frac{\lambda_y}{2}(\partial_y h)^2. \quad (2)$$

Here, ν_x,ν_y, and K are the coefficients as for (1). λ_x,λ_y incorporate the dependence of the erosion rate on the local incidence angle. The aKS equation predicts for $\nu_x < \nu_y < 0$ the growth of a parallel ripple mode at early times, which will eventually saturate [44,47–49]. Numerical simulations by Keller *et al.* [49] for $\lambda_x \gg \lambda_y > 0$ show the emergence of a perpendicular mode in qualitative agreement with the surface morphology in the high-fluence regime observed here for $\vartheta = 63^\circ$.

The evolution in the $\vartheta = 75^\circ$ high-fluence regime is qualitatively different from the one at $\vartheta = 63^\circ$. We attribute the formation of the roof-tile structure accompanied by strong coarsening and disordering of the pattern to nonlocal effects. As partial differential equations for the height evolution are inherently local, such effects can not be captured by them. The nonlocal effect under concern here is the reflection of ions, such that they hit the sample again at a distant location. We note that redeposition has recently been included into a new type of *nonlocal* continuum modeling resulting in a partial integrodifferential equation for the surface evolution [50,51],

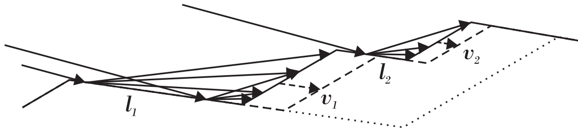

FIG. 11. Sketch to illustrate coarsening by reflected ions. See text.

but the effect of reflected ions and the sputtering associated with them has so far been neglected.

Indeed, for grazing incidence angles, the overwhelming fraction of ions experiences only small angle scattering through surface atoms, i.e., the projectiles do not penetrate the surface, but are reflected with little energy loss by the surface layer atoms [52]. The reflected ions may hit surface features in their path of flight and thereby can contribute substantially to sputtering [53]. Based on his observations for 10 keV Ar^+ ion exposure of Ag crystals, Hauffe [54] proposed that sputtering through reflected ions is the origin of rapid coarsening. The Hauffe mechanism has also been invoked to explain the strong coarsening observed for the Ge(001) morphology upon 1.2 keV Xe^+ exposure with $\vartheta = 75^\circ$ [42]. The same mechanism is considered here to be responsible for the rapid coarsening in the surface morphological evolution under $\vartheta = 75^\circ$ 2 keV Kr^+ exposure of Si(001).

Consider ions impinging on the downwind faces of Si(001) as indicated in Fig. 11. According to Fig. 8(d), the 2 keV Kr^+ impinge for $\vartheta = 75^\circ$ with a local angle $\theta \geqslant 82^\circ$ on the downwind faces. Based on TRIM.SP calculations, under these conditions, ≈80% of the ions are reflected at the surface layer and predominantly scattered with little energy loss into grazing directions with a small angular spread. Therefore such particles hit an adjacent upwind face with substantial probability and enhance the erosion of these faces. The additional flux of reflected ions onto a given upwind face is enhanced the stronger, the larger the feeding downwind face. Therefore the large (small) downwind face with length l_1 (l_2) gives rise to a large (small) erosion ion speed v_1 (v_2) of the adjacent upwind face, as shown in Fig. 11. In consequence, a larger downwind face will grow at the expense of a smaller one, until the smaller one vanishes (compare Fig. 11). This coarsening mechanism prefers the formation of large downwind faces, but it does not select a specific structure size. Thus the order of the surface is expected to decline with continued erosion, as observed.

To estimate the relevance of the Hauffe mechanism in the high-fluence regime, we calculated the flux ratio $r = \Phi_r/\Phi_p$ of ions reflected onto the upwind face to primary ions hitting it directly. Assuming specular reflection for simplicity, the flux ratio is $r = R(\theta_d)\cos(\theta_r)/\cos(\theta_u)$, where $R(\theta_d)$ is the ion reflectivity as a function of the local incidence angle on the downwind face, $\theta_r = 180^\circ - \vartheta - \alpha_u - 2\alpha_d$ is the local incidence angle of reflected ions on the upwind face, $\theta_{d,u} = \vartheta \pm \alpha_{d,u}$ are the local incidence angles of the primary ion on the downwind and upwind faces and $\alpha_{d,u}$ are the slope angles of the downwind and upwind faces. For $\vartheta = 63^\circ$, the reflectivity $R < 0.3$ at the downwind face leads to a flux enhancement $r < 0.01$ and the effect of reflected ions on the morphological evolution must be considered to be minor. For $\vartheta = 75^\circ$, the reflectivity of the downwind face is $R \approx 0.8$ in the high-fluence regime. The resulting flux enhancement of $r \approx 0.6$ is substantial and certainly sufficient to trigger the observed coarsening.

The well defined faces observed in the high-fluence regime for $\vartheta = 75^\circ$ suggest that gradient-dependent sputtering might be relevant for this regime. Indeed, Carter *et al.* [55] showed that faces with local incidence angles of 0°, 90°, and θ_{max} (the angle of the maximum sputtering yield) are the only stable ones, if only the dependence of the sputtering yield $Y(\theta)$ on θ is taken into account for modeling surface evolution. In striking contrast to these predictions, in the $\vartheta = 75^\circ$ high-fluence regime, the local incidence angle on the upwind face is $\theta \approx 50^\circ$, far away from both, the maximum of the sputtering yield at $\theta = 72^\circ$, as calculated with TRIM.SP [56], and from $\theta = 0^\circ$. Likewise, the local incidence angle on the downwind face is $\theta \approx 82^\circ$, distinctly different from 90°. Consequently, the local incidence angles of the faces in the $\vartheta = 75^\circ$ high-fluence regime cannot be accounted for by the theory of Carter *et al.* [55].

Geometric shadowing has been used by Carter [57] to explain the formation of sawtooth profiles upon grazing ion incidence and subsequently invoked as an explanation for such profiles at low ion energy by Gago *et al.* [58] and medium ion energy by Datta and Chini [59]. According to Carter [57], shadowing sets in for a sinusoidal ripple profile, when the steepest slope of the downwind face becomes parallel to the ion beam (compare Fig. 1 of Ref. [57]). Indeed, as visible in the height profile of Fig. 10(i) with the properly indicated ion beam direction, at the end of the 75° low-fluence regime, the downwind face reaches occasionally a local slope angle of 15°, making this portion of the surface parallel to the ion beam. Therefore, instead of assuming the onset of ion reflection to be decisive for the transition to the high-fluence regime, one might argue that the onset of geometric shadowing is the decisive effect.

However, as visible from the height profile in Fig. 10(k) with the properly indicated ion beam direction, in the high-fluence regime, the downwind faces never become parallel to the ion beam, i.e., the local incidence angle never reaches 90°. For the downwind face in the height profile of Fig. 10(k) after $F = 3.0 \times 10^{22}$ ions/m^2 the local incidence angle is 79°, i.e., the angle between the ion beam and the downwind face is still 11°. This substantial angle is also highlighted through the properly scaled ion beam direction indicated in Fig. 10(k). An angle of 11° between the downwind face and the ion beam is a typical value. This statement is underlined by Fig. 8(d), which displays for the 75° high-fluence regime local incidence angles θ_d between 83.9° and 81.5°. These are local incidence angles for the locations of *maximum* slope α_d, while the local incidence angles on the flat parts of the downwind faces are smaller by ≈3° (compare Fig. 1 and related discussion). Thus it appears that the concept of geometric shadowing can not be applied without modifications to explain the transition from low-fluence to high-fluence regime for $\vartheta = 75^\circ$.

In Secs. III B and III C, it was found that $\alpha_d = 8^\circ$ for both high-fluence regimes, the 63° and the 75° one. This seems to indicate that α_d is pinned to the flat surface orientation rather than to the ion beam direction. To test this hypothesis, we analyzed α_d and α_u for the broad angular range from 58° to 77°. The results are shown in Fig. 12, where the global incidence angle ϑ is indicated by a dashed line. Indeed,

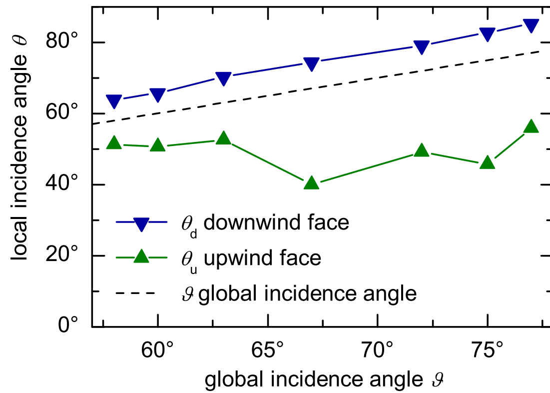

FIG. 12. (Color online) Local incidence angle on downwind face θ_d and upwind face θ_u as a function of global incidence angle ϑ.

the local incidence angle on the downwind face evolves with a fixed angular separation of 8° with respect to ϑ for $63^\circ \leqslant \vartheta \leqslant 77^\circ$. This separation is nothing but the local slope α_d. Therefore, in this angular range, there is a magic downwind surface slope, independent of the ion beam incidence angle ϑ. For smaller ϑ, the separation is a little lower ($\approx 6^\circ$), possibly because pattern saturation is not yet reached. On the upwind face, the local incidence angle scatters somewhat. It is less well defined due to the broader angular distribution on this face (compare Figs. 6 and 10). Nevertheless, the local incidence angle apparently remains fixed at $\theta_u \approx 50^\circ$. This implies a simultaneous increase of the upwind surface slope α_u and ϑ. In conclusion, the upwind face is pinned to the ion beam direction, while the downwind face is pinned to the global surface orientation. We have no explanation for this remarkable behavior, but believe that it might stimulate additional research. Finally, we note that the downwind face orientation being pinned to the global surface orientation rather than the ion beam direction appears to be hardly compatible with geometric shadowing being of relevance.

As a last issue, one might hypothesize that by prolonged ion exposure beyond the maximum fluence of $F = 9.5 \times 10^{22}$ ions/m^2 used in this study, it could be possible to transform the ripple pattern at $\vartheta = 63^\circ$ into a roof-tile pattern. A rational basis for such a hypothesis could be seen in the fact that for both angular ranges the low-fluence regime is similar, dominated by a parallel mode ripple pattern. However, the hypothesis appears unlikely to be valid, when considering that the key difference between the two high-fluence regimes is ion reflection and the sputtering associated with it. The stable local incidence angles at $\vartheta = 63^\circ$ [compare Fig. 8(d)] together with a negligible flux enhancement on the upwind face (a factor of 60 smaller as for the $\vartheta = 75^\circ$ case, according to our calculations) suggests the Hauffe mechanism to be largely inoperative at $\vartheta = 63^\circ$. On a more descriptive level, λ, and the parallel mode ripple pattern roughness σ_s are stationary at the end of the investigated fluence range for $\vartheta = 63^\circ$. There is no indication that this behavior will change, as it would be necessary to display the rapid increase of λ and σ in the high-fluence regime at $\vartheta = 75^\circ$.

To obtain a quantitative insight on how well the results of various ion beam exposure experiments of Si(001) match and how strongly they depend on ion beam parameters, we collected data from the literature [11,34–36] for the angular ranges of ripple pattern and roof-tile pattern formation and display them in Fig. 13. As no two data sets represented in Figs. 13(a) and 13(b) agree in all parameters (incidence angle ϑ, ion species, ion energy), no perfect agreement can be expected between any of the experiments. As an additional note of caution, we remark that Basu *et al.* [11], Castro *et al.* [31], Madi *et al.* [34], Keller *et al.* [35], and Zhang *et al.* [36] conducted their erosion experiments for samples with a native oxide layer. Sputtering SiO_2 rather than Si at low fluences (up to a few times 10^{19} ions/m^2) may affect the initial stages of the morphological evolution.

We start with a discussion of Fig. 13(a), where roughness data are compared to our $\vartheta = 63^\circ$ sequence in the ripple pattern range. Despite some experimental scatter, it is obvious that the roughness data from Keller *et al.* [35] for 500 eV Ar^+ at $\vartheta = 67^\circ$ match surprisingly well to our measurement with 2 keV Kr^+ at $\vartheta = 63^\circ$. Moreover, Keller *et al.* [35] observed the same sequence of patterns as we did. First, a parallel mode ripple pattern evolves. Then, simultaneously with the saturation of this mode, beyond a critical fluence, a disordered perpendicular mode develops, which eventually

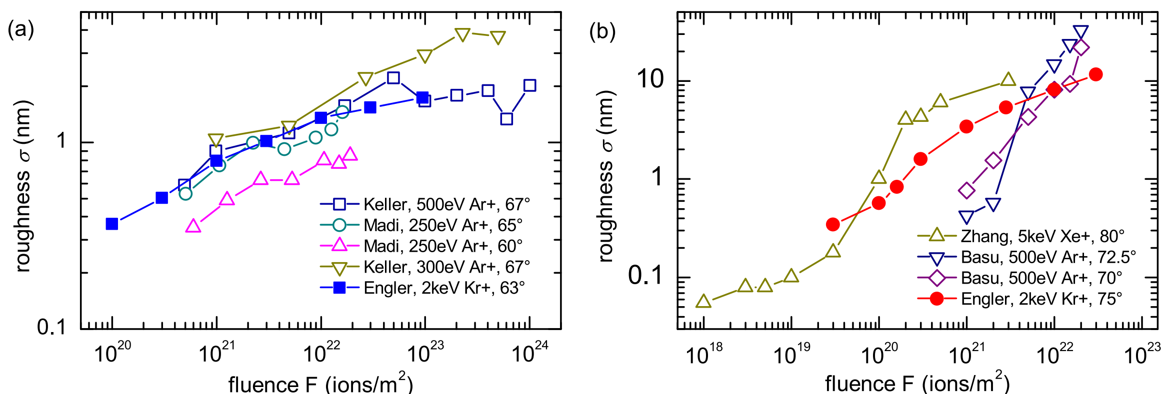

FIG. 13. (Color online) Roughness σ as a function of ion fluence F for ion exposure of Si(001) under various ion beam conditions. (a) Experimental data by Keller *et al.* [35] and Madi *et al.* [34] suitable for comparison to the $\vartheta = 63^\circ$ data of the present study in the ripple pattern range. (b) Experimental data by Basu *et al.* [11] and Zhang *et al.* [36] suitable for comparison to the $\vartheta = 75^\circ$ data of the present study in the roof-tile range.

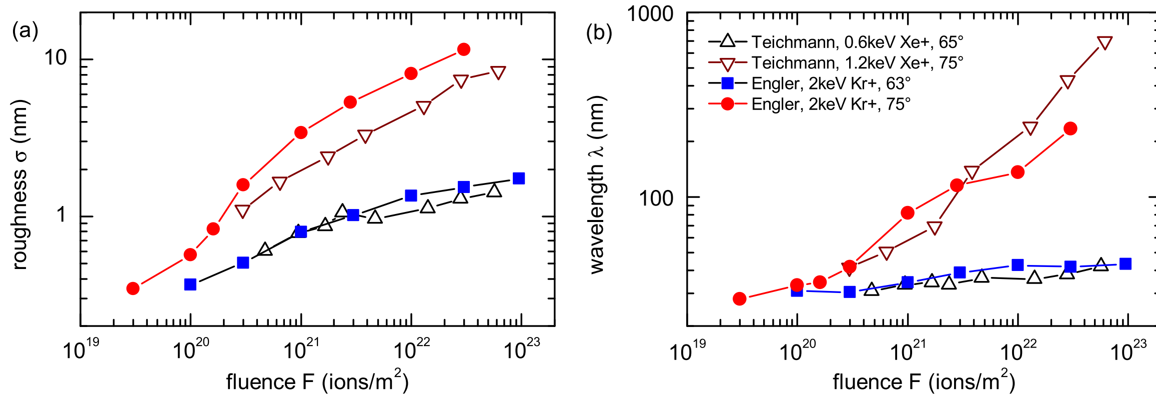

FIG. 14. (Color online) Evolution of (a) roughness σ and (b) wavelength λ of ion beam induced patterns on Si and Ge (Teichmann *et al.* [42]) as a function of fluence.

dominates the roughness. Only the critical fluences for the onset of the disordered perpendicular mode are substantially higher for 300 eV and 500 eV Ar^+ exposure compared to 2 keV Kr^+. The sequence of patterns observed by Castro *et al.* [31] for 500 eV Ar^+ at $\vartheta = 65^\circ$ is again identical to the one observed by us, but for this case the authors do not provide quantitative roughness data that could be represented in Fig. 13(a). Madi *et al.* [34] vary the fluence of 250 eV Ar^+ ions only by a factor of 30. The roughness evolution at $\vartheta = 65^\circ$ matches rather well with our results for 2 keV Kr^+ at $\vartheta = 63^\circ$. However, apparently, the roughness develops nonmonotonically with ion fluence. Moreover, no topographic images are shown and thus a straightforward comparison to our patterns is not possible.

In Fig. 13(b), roughness data in the roof-tile pattern range are compared to our $\vartheta = 75^\circ$ sequence. The data set of Zhang *et al.* [36] for 5 keV Xe^+ at $\vartheta = 80^\circ$ and to a lesser extent the 500 eV Ar^+ at $\vartheta = 72.5^\circ$ data of Basu *et al.* [11] display a similar S-shaped roughness curve as our 2 keV Kr^+ at $\vartheta = 63^\circ$ data set. Specifically, also for 5 keV Xe^+ the low-fluence regime may be fitted rather well through an exponential growth of the roughness, as for 2 keV Kr^+. In both studies [11,36], the sequence of the morphologies is qualitatively similar to our 2 keV Kr^+ case. Parallel mode ripples transform into a roof-tile morphology with the tips of the roof tiles pointing into the direction of the ion beam. In all cases, the evolution of the roof-tile pattern is accompanied by strong coarsening. The transition fluences from the low-fluence ripple to the high-fluence roof-tile pattern almost agree quantitatively between the study of Zhang *et al.* [36] and our experiments. Despite these similarities, Fig. 13(b) displays also marked differences in roughness evolution for the different data sets. Zhang *et al.* [36] measure surprisingly low roughnesses down to $\sigma = 0.06$ nm for very low fluences, where the sample morphology is possibly affected by SiO_2. Although Basu *et al.* [11] only vary the ion fluence by a factor of 20, their roughness increases for 500 eV Ar^+ at $\vartheta = 72.5^\circ$ in absolute numbers more than in our experiments, where the ion fluence is varied by a factor of 1000.

Recently, Teichmann *et al.* [42] demonstrated the entire absence of pattern formation on Ge(001) after low-energy Ne^+ or Ar^+ exposure. This raises the question, whether Si and Ge behave entirely different under ion beam exposure due to differences in their material properties. Therefore we compare in Figs. 14(a) and 14(b) our data for roughness evolution and wavelength, respectively, with the corresponding data of Teichmann *et al.* [42] for 600 eV Xe^+ at $\vartheta = 65^\circ$ and 1.2 keV Xe^+ at $\vartheta = 75^\circ$. The fluences of Ref. [42] are scaled by $\cos\vartheta$ as they were originally stated with respect to a plane perpendicular to the ion beam. For the ripple pattern range, we have to compare the 600 eV Xe^+ at $\vartheta = 65^\circ$ data set with our 2 keV Kr^+ at $\vartheta = 63^\circ$ sequence. Figure 14 immediately tells that roughness evolution and the magnitude and constancy of the wavelength are strikingly similar for the two data sets. Also the morphological evolution as apparent in the AFM topographs displayed by Teichmann *et al.* [42] is very similar. First, a parallel ripple mode evolves and saturates, on top of which beyond a critical fluence a disordered perpendicular mode develops, which eventually dominates the surface roughness. The disordered perpendicular mode develops at a fluence of $F \approx 2 \times 10^{21}$ ions/m^2 close to the fluence $F \approx 3 \times 10^{21}$ ions/m^2 observed here for Si. For the roof-tile range of incidence angles, Fig. 14 compares the 1.2 keV Xe^+ at $\vartheta = 75^\circ$ data set for Ge(001) with our 2 keV Kr^+ at $\vartheta = 75^\circ$ sequence for Si(001). Both data sets display similar roughness and wavelength evolution, although the absolute numbers differ, not unexpectedly. Also qualitatively, based on the AFM data of Teichmann *et al.* [42], the evolution is similar to the Si one. The low-fluence parallel ripple mode is followed by the evolution of a roof-tile-structure, which is accompanied by strong coarsening and disordering. Finally, we note that for Ge also the smooth flat surface morphology for incidence angles ϑ below the onset of ripple pattern formation exists. Likewise, also the grazing morphology with faint grooves in ion beam direction for grazing incidence beyond the roof-tile pattern is observed on Ge (compare Ref. [4] for Si). We conclude that the angular ranges of ripple pattern and roof-tile pattern formation, as well as the regimes of low and high fluence are a universal feature in ion beam erosion of Si and Ge surfaces.

V. CONCLUSION

Using 2 keV Kr^+ incident on Si(001), we find two ranges of pattern formation, the ripple pattern range extending from $58^\circ \leqslant \vartheta \leqslant 63^\circ$ and the roof-tile pattern range extending from $67^\circ \leqslant \vartheta \leqslant 79^\circ$. We investigated the fluence dependence in these two ranges at 63° and 75°. Both types of pattern display distinct low and high-fluence regimes.

For 63°, an ordered parallel mode ripple pattern of fixed wavelength evolves in the low-fluence regime. This pattern saturates in amplitude and ripple shape, and in the high-fluence regime beyond a few 10^{21} ions/m^2, a disordered, long-wavelength perpendicular mode evolves that eventually dominates morphology and roughness of the system.

Also at 75°, an ordered parallel mode ripple pattern with only slightly increasing wavelength evolves in the low-fluence regime. Already at $\approx 5 \times 10^{20}$ ions/m^2, the system enters the high-fluence regime. Then, the initial ripple pattern rapidly transforms into a roof-tile structure, formed by extended flat downwind faces and short, steep upwind faces. The formation of the roof-tile structure is accompanied by strong coarsening, disordering and roughness increase.

The morphological evolution in the low-fluence regimes is for both angular ranges similar. The evolution of a parallel mode ripple pattern with nearly fixed wavelength, an exponential roughness increase and an improvement of the pattern order with fluence all indicate that the initial system evolution may be described by a linear partial equation of the type first used by Bradley and Harper [24] to reasonable approximation.

The morphological evolution in the high-fluence regimes is for both angular ranges distinctively different. At $\vartheta = 63°$, it is characterized by a saturated parallel ripple mode and the evolution of a perpendicular mode indicates the presence of nonlinear effects that may be accounted for through a description with a nonlinear partial differential equation, like the anisotropic Kuramato-Sivashinsky equation [46,49]. At $\vartheta = 75°$, it is characterized by the formation of a roof-tile structure, which is unaccessible to a description by partial differential equations because of the dominance of nonlocal effects. The overwhelming fraction of ions impinging on the downwind face is reflected and hits subsequently the upwind face, where it causes sputtering. Though a detailed understanding of the morphology is out of reach yet, this nonlocal effect, known as Hauffe-mechanism [54], is the origin of the rapid coarsening and disordering.

Based on an analysis of the local surface slopes, geometric shadowing appears to be inoperative for the transition from the low to the high-fluence regime in the roof-tile pattern range. In the high-fluence regime, the local ion beam incidence angle on the downwind face stays always well below 90°. Interestingly, in the roof-tile pattern range, the slope of the downwind face is fixed, independent on the ion incidence angle. To the contrary, the slope of the upwind face increases simultaneously with ϑ, i.e., it is pinned to the ion beam orientation. These unexpected findings might stimulate future investigation.

Based on our comparison to the existing data, we conclude that the distinct angular ranges of no pattern formation and of pattern formation, as well as the distinctly different regimes of low and high fluence are not only universal features for ion beam erosion of Si, but for Ge as well. While it is well known that for multicomponent materials new phenomena of pattern formation arise [14], it is an interesting experimental task to analyze, whether the phenomenology and the terminology presented here fits also for the description of other single component materials that are amorphous or amorphize under ion beam exposure, e.g., for amorphous carbon [12].

In conclusion, we are convinced that our comprehensive study, conducted under well defined conditions, substantially contributes to establish an experimental basis and phenomenological distinctions that will help to make the richness of ion beam erosion patterns better accessible to a physical understanding and theoretical description.

ACKNOWLEDGMENTS

F. F. thanks Marc Teichmann for useful discussions. This work was supported by Deutsche Forschungsgemeinschaft (DFG) through Forschergruppe 845.

[1] M. Navez, C. Sella, and D. Chaperot, Comptes Rendus Hebdomadaires Des Seances De L Academie Des Sciences **254**, 240 (1962).

[2] S. Facsko, T. Dekorsy, C. Koerdt, C. Trappe, H. Kurz, A. Vogt, and H. L. Hartnagel, Science **285**, 1551 (1999).

[3] T. Michely, M. Kalff, G. Comsa, M. Strobel, and K.-H. Heinig, Phys. Rev. Lett. **86**, 2589 (2001).

[4] S. Macko, F. Frost, B. Ziberi, D. F. Förster, and T. Michely, Nanotechnol. **21**, 085301 (2010).

[5] S. Macko, F. Frost, M. Engler, D. Hirsch, T. Höche, J. Grenzer, and T. Michely, New. J. Phys. **13**, 073017 (2011).

[6] S. Macko, J. Grenzer, F. Frost, M. Engler, D. Hirsch, M. Fritzsche, A. Mücklich, and T. Michely, New J. Phys. **14**, 073003 (2012).

[7] F. Frost, A. Schindler, and F. Bigl, Phys. Rev. Lett. **85**, 4116 (2000).

[8] J. Völlner, B. Ziberi, F. Frost, and B. Rauschenbach, J. Appl. Phys. **109**, 043501 (2011).

[9] X. Ou, A. Keller, M. Helm, J. Fassbender, and S. Facsko, Phys. Rev. Lett. **111**, 016101 (2013).

[10] J. Muñoz-García, R. Gago, R. Cuerno, J. A. Sánchez-García, A. Redondo-Cubero, M. Castro, and L. Vázquez, J. Phys.: Condens. Matter **24**, 375302 (2012).

[11] T. Basu, D. Datta, and T. Som, Nanoscale Res. Lett. **8**, 289 (2013).

[12] O. Bobes, K. Zhang, and H. Hofsäss, Phys. Rev. B **86**, 235414 (2012).

[13] A. Keller, S. Facsko, and W. Möller, J. Phys.: Condens. Matter **21**, 495305 (2009).

[14] M. Engler, F. Frost, S. Müller, S. Macko, M. Will, R. Feder, D. Spemann, R. Hübner, S. Facsko, and T. Michely, Nanotechnol. **25**, 115303 (2014).

[15] B. Ziberi, M. Cornejo, F. Frost, and B. Rauschenbach, J. Phys.: Condens. Matter **21**, 224003 (2009).

[16] B. Poelsema, L. K. Verheij, and G. Comsa, Phys. Rev. Lett. **53**, 2500 (1984).

[17] B. Poelsema, R. Kunkel, L. K. Verheij, and G. Comsa, Phys. Rev. B **41**, 11609 (1990).

[18] T. Michely and G. Comsa, Phys. Rev. B **44**, 8411 (1991).

[19] T. Michely and G. Comsa, Nucl. Instrum. Methods Phys. Res., Sect. B **82**, 207 (1993).
[20] M. Kalff, G. Comsa, and T. Michely, Surf. Sci. **486**, 103 (2001).
[21] M. Strobel, K.-H. Heinig, and T. Michely, Surf. Sci. **486**, 136 (2001).
[22] H. Hansen, A. Redinger, S. Messlinger, G. Stoian, Y. Rosandi, H. M. Urbassek, U. Linke, and T. Michely, Phys. Rev. B **73**, 235414 (2006).
[23] S. J. Chey, J. E. Van Nostrand, and D. G. Cahill, Phys. Rev. B **52**, 16696 (1995).
[24] R. M. Bradley and J. M. E. Harper, J. Vac. Sci. Technol. A **6**, 2390 (1988).
[25] G. Ozaydin, A. S. Özcan, Y. Wang, K. F. Ludwig, H. Zhou, R. L. Headrick, and D. P. Siddons, Appl. Phys. Lett. **87**, 163104 (2005).
[26] C. S. Madi, B. Davidovitch, H. B. George, S. A. Norris, M. P. Brenner, and M. J. Aziz, Phys. Rev. Lett. **101**, 246102 (2008).
[27] C. S. Madi and M. J. Aziz, Appl. Surf. Sci. **258**, 4112 (2012).
[28] P. Sigmund, J. Mater. Sci. **8**, 1545 (1973).
[29] G. Carter and V. Vishnyakov, Phys. Rev. B **54**, 17647 (1996).
[30] M. Castro and R. Cuerno, Appl. Surf. Sci. **258**, 4171 (2012).
[31] M. Castro, R. Gago, L. Vázquez, J. Muñoz-García, and R. Cuerno, Phys. Rev. B **86**, 214107 (2012).
[32] S. A. Norris, M. P. Brenner, and M. J. Aziz, J. Phys.: Condens. Matter **21**, 224017 (2009).
[33] S. A. Norris, J. Samela, L. Bukonte, M. Backman, F. Djurabekova, K. Nordlund, C. S. Madi, M. P. Brenner, and M. J. Aziz, Nat. Commun. **2**, 276 (2011).
[34] C. S. Madi, H. B. George, and M. J. Aziz, J. Phys.: Condens. Matter **21**, 224010 (2009).
[35] A. Keller, S. Roßbach, S. Facsko, and W. Möller, Nanotechnol. **19**, 135303 (2008).
[36] K. Zhang, H. Hofsäss, F. Rotter, M. Uhrmacher, C. Ronning, and J. Krauser, Surf. Coat. Technol. **203**, 2395 (2009).
[37] A. H. Al-Bayati, K. G. Orrman-Rossiter, J. van den Berg, and D. Armour, Surf. Sci. **241**, 91 (1991).
[38] I. Horcas, R. Fernandez, J. M. Gomez-Rodriguez, J. Colchero, J. Gomez-Herrero, and A. M. Baro, Rev. Sci. Instrum. **78**, 013705 (2007).
[39] D. Nečas and P. Klapetek, Cent. Eur. J. Phys. **10**, 181 (2012).
[40] E. Vivo, M. Nicoli, M. Engler, T. Michely, L. Vázquez, and R. Cuerno, Phys. Rev. B **86**, 245427 (2012).
[41] See Supplemental Material at http://link.aps.org/supplemental/10.1103/PhysRevB.89.245412 for STM topographs in the incidence angle range $60^\circ \leqslant \vartheta \leqslant 81^\circ$.
[42] M. Teichmann, J. Lorbeer, B. Ziberi, F. Frost, and B. Rauschenbach, New J. Phys. **15**, 103029 (2013).
[43] R. M. Bradley, Phys. Rev. B **84**, 075413 (2011).
[44] M. A. Makeev, R. Cuerno, and A.-L. Barabási, Nucl. Instrum. Methods Phys. Res., Sect. B **197**, 185 (2002).
[45] S. A. Norris, Phys. Rev. B **85**, 155325 (2012).
[46] R. Cuerno and A.-L. Barabási, Phys. Rev. Lett. **74**, 4746 (1995).
[47] M. Rost and J. Krug, Phys. Rev. Lett. **75**, 3894 (1995).
[48] S. Park, B. Kahng, H. Jeong, and A.-L. Barabási, Phys. Rev. Lett. **83**, 3486 (1999).
[49] A. Keller, M. Nicoli, S. Facsko, and R. Cuerno, Phys. Rev. E **84**, 015202 (2011).
[50] C. Diddens and S. J. Linz, Europhys. Lett. **104**, 17010 (2013).
[51] R. M. Bradley, Phys. Rev. B **83**, 075404 (2011).
[52] A. Boers, Surf. Sci. **63**, 475 (1977).
[53] A. Redinger, Y. Rosandi, H. M. Urbassek, and T. Michely, Phys. Rev. B **77**, 195436 (2008).
[54] W. Hauffe, Phys. Stat. Sol. (a) **35**, K93 (1976).
[55] G. Carter, J. S. Colligon, and M. J. Nobes, J. Mater. Sci. **6**, 115 (1971).
[56] W. Eckstein, Radiat. Eff. Defects Solids **130**, 239 (1994).
[57] G. Carter, J. Appl. Phys. **85**, 455 (1999).
[58] R. Gago, L. Vázquez, R. Cuerno, M. Varela, C. Ballesteros, and J. M. Albella, Nanotechnol. **13**, 304 (2002).
[59] D. P. Datta and T. K. Chini, Phys. Rev. B **76**, 075323 (2007).